

# The combined X-ray and $\gamma$ -ray modeling of millisecond pulsars PSR J0030+0451 in the dissipative magnetospheres

GANG CAO<sup>1</sup> AND XIONGBANG YANG<sup>1</sup>

<sup>1</sup>Department of Mathematics, Yunnan University of Finance and Economics, Kunming 650221, Yunnan, P. R. China;  
 gcao@ynufe.edu.cn, xbyang@ynufe.edu.cn

## ABSTRACT

Modeling of the NICER X-ray light curves of millisecond pulsars PSR J0030+0451 provides a strong evidence for the existence of non-dipole magnetic fields. We study the X-ray and  $\gamma$ -ray emission of PSR J0030+0451 in the dissipative dipole plus off-centred quadrupole magnetospheres. The dissipative FF+AE dipole magnetospheres by combining force-free (FF) and Aristotelian electrodynamics (AE) are solved by a 3D pseudo-spectral method in the rotating coordinate system. We use the FF+AE dipole plus off-centred quadrupole fields with minimum free parameters to reproduce two hotspot configurations found by the NICER observations. The X-ray and  $\gamma$ -ray emission from PSR J0030+0451 are simultaneously computed by using a ray-tracing method and a particle trajectory method. The modelled X-ray and  $\gamma$ -ray emission is then directly compared with those of PSR J0030+0451 from the NICER and Fermi observations. Our results can well reproduce the observed trends of the NICER X-ray and Fermi  $\gamma$ -ray emission for PSR J0030+0451.

*Keywords:* magnetic field - method: numerical - gamma-ray: star - pulsars: general

## 1. INTRODUCTION

Pulsars are thought to be rapidly rotating and highly magnetized neutron stars. Millisecond pulsars (MSPs) are a class of the old pulsars with short rotation periods in the range of 1 – 30 ms. They have low surface magnetic fields with the order of  $B \sim 10^8$  G and small spin-down rates with the order of  $\dot{P} \sim 10^{-20}$  compared to the young pulsars. These objects can produce the multi-wavelength electromagnetic spectra from the radio up to  $\gamma$ -ray bands. The  $\gamma$ -ray emission are expected to originate from well above the neutron star surface, the Fermi  $\gamma$ -ray emission can thus be used to diagnose the structure of the outer magnetosphere. The thermal X-ray emission would originate from the hotspot regions of the neutron star surface, which can provide a excellent probe of surface magnetic field structure. Therefore, the combined X-ray and  $\gamma$ -ray modeling can put the strong constraints on the magnetic field configuration of MSPs.

Recently, Neutron Star Interior Composition Explorer (NICER) is accurately measuring the X-ray light emission of MSPs. One of the first NICER targets is the MSP PSR J0030+0451 with the rotation period of  $P = 4.87$  ms, which is also the first  $\gamma$ -ray MSP observed by Fermi-LAT (Abdo et al. 2019). The light curves from the NICER observations show double-peak X-ray profiles with  $\sim 180^\circ$  peak separation. The detailed fitting of the X-ray light curves precisely constrain the

mass and radius of the neutron star with the surface hotspot models (Riley et al. 2019; Miller et al. 2012). They present two hotspot models with a circular shape and a crescent shape in the southern hemisphere. Such a configuration provides a strong evidence for the existence of non-dipolar surface magnetic field, because the dipole fields produces two near-circular antipodal hotspots. The hotspots are expected to be heated by high-energy particles from the magnetospheres. The hotspot shapes is determined by the footprints of the open magnetic field lines, which is related to the structure of the global pulsar magnetospheres. Therefore, the key to understand the X-ray and  $\gamma$ -ray emission is to solve the complicated magnetospheric configurations.

Significant advances have been achieved towards the self-consistent modeling of the pulsar magnetospheres. The vacuum magnetosphere is the first solution to describe the global pulsar magnetosphere (Deutsch 1955), which can provide a reference solution to understand more complicated magnetospheric structures thanks to the analytic expression. It is well established that the pulsar magnetospheres should be the plasma-filled magnetospheres with plasmas from the pair production (Goldreich & Julian 1969). A zeroth-order approximation FF model is developed to construct the plasma-filled magnetospheres (Contopoulos et al. 1999; Spitkovsky 2006; Kalapotharakos & Contopoulos 2009; Contopoulos

los & Kalapotharakos 2010; Pétri 2012; Cao et al. 2016a; Pétri 2016; Carrasco et al. 2018; Kim et al. 2024; Dimitropoulos & Contopoulos 2025; Skiathas et al. 2025), which can precisely describe the magnetic field geometry by including the modification of plasma currents on the field structure. However, the FF solutions can not accelerate the particles to produce the observed pulsed emission. The dissipative resistive models are then developed to model the pulsar magnetosphere with a prescribed conductivity (Li et al. 2012; Kalapotharakos et al. 2012; Cao et al. 2016b; Pétri 2025), which can introduce the local accelerating electric field to produce the observed pulsed emission. However, there are no clear physical motivation for these arbitrary conductivity in the resistive model. The kinetic particle-in-cell (PIC) methods are later developed to address the microscopic physical processes of particle acceleration and creation (Philippov et al. 2015; Cerutti et al. 2016; Kalapotharakos et al. 2018; Brambilla et al. 2018; Soudais 2024). However, the PIC method can not use real pulsar parameters to compute the pulsar magnetosphere and predict the pulsar  $\gamma$ -ray emission due to the large separation between the macroscopic scales to the microscopic scales. Both resistive and PIC simulations produce a near FF magnetosphere with a current sheet outside the light cylinder, and the current sheet is suggested to be the main site of particle acceleration and  $\gamma$ -ray emission (Bai & Spitkovsky 2010; Kalapotharakos et al. 2014; Harding & Kalapotharakos 2015; Cerutti et al. 2016; Philippov & Spitkovsky 2018; Cao & Yang 2019; Yang & Cao 2021; Harding et al. 2021; Kalapotharakos et al. 2023). Recently, a new FF+AE model is proposed to construct the pulsar magnetosphere (Contopoulos et al. 2016; Pétri 2020a; Cao & Yang 2020; Pétri 2022; Cao et al. 2024a), which can produce a near FF solution with the accelerating electric field only near the current sheet. Moreover, the FF+AE model can use real pulsar parameters to predict the pulsar  $\gamma$ -ray emission.

The multiwavelength emission of PSR J0030+0451 have been studied based on different magnetospheric models (Chen et al. 2020; Kalapotharakos et al. 2021; Carrasco et al. 2023; Pétri et al. 2023a). Pétri et al. (2023a) used a vacuum dipole plus off-centred dipole magnetosphere to model the radio and  $\gamma$ -ray emission of PSR J0030+0451. Carrasco et al. (2023) used a FF dipole magnetosphere to model the X-ray emission of PSR J0030+0451, while Fermi  $\gamma$ -ray emission is not simultaneously modeled in their study. Chen et al. (2020) used a FF dipole plus off-centred quadrupole magnetospheres to model the X-ray and  $\gamma$ -ray emission of PSR J0030+0451, where a uniform emissivity modu-

lated by the local parallel force-free current is assumed to compute the  $\gamma$ -ray emission. Kalapotharakos et al. (2021) used an off-centred FF dipole plus off-centred quadrupole magnetospheres to model the X-ray and  $\gamma$ -ray of PSR J0030+0451. However, they only used an approximate accelerating electric field scaled with a finite conductivity to compute  $\gamma$ -ray emission. In fact, the  $\gamma$ -ray emission of PSR J0030+0451 is not self-consistently computed by using the accelerating electric fields from magnetosphere simulation in all these studies. It is shown that the Fermi observed features of the pulsar  $\gamma$ -ray emission can generally be reproduced by the FF+AE magnetospheres (Cao & Yang 2022, 2024b). Moreover, the FF+AE magnetosphere can also generally reproduced the observed trends of the pulsar multiwavelength emission from the optical to TeV  $\gamma$ -ray bands (Yang & Cao 2024). Motivated by agreement of the FF+AE magnetospheres with observations, we use a FF+AE dipole plus off-centred quadrupole magnetosphere to explore the X-ray and  $\gamma$ -ray emission of PSR J0030+0451, where the  $\gamma$ -ray emission of PSR J0030+0451 is self-consistently computed by using the accelerating electric fields from the FF+AE magnetospheric simulations. In this paper, we use a FF+AE dipole plus off-centred quadrupole fields to obtain the polar cap shapes similar to the NICER observation results. A ray-tracing method is developed to compute the thermal X-ray emission, and a particle trajectory method is used to self-consistently compute the  $\gamma$ -ray emission from curvature radiation based on the accelerating electric field from magnetosphere simulation. The predicted X-ray and  $\gamma$ -ray emission is then directly compared with the NICER and Fermi observation for PSR J0030+0451.

## 2. MAGNETOSPHERIC MODELS

In our model, the FF+AE dipole magnetospheres by combining the FF and AE method are computed by a 3D spectral code for a range of dipole inclination angles, the vacuum dipole plus off-centred quadrupole field is firstly used to find a range of initial dipole and quadrupole parameters with the polar caps similar to the NICER results, these initial dipole and quadrupole parameters are then used to construct a range of the FF+AE dipole plus off-centred quadrupole magnetospheres, the final parameter solutions for the FF+AE dipole plus off-centred quadrupole magnetospheres are determined by simultaneously fitting the NICER X-ray and Fermi  $\gamma$ -ray emission.

### 2.1. Vacuum Dipole and Off-centred Quadrupole Magnetospheres

The pulsar magnetospheres are expected to be the plasma-filled magnetospheres instead of the vacuum magnetospheres. However, the vacuum magnetosphere can be served as a reference solution to explore more complicated field configuration thanks to the analytic expression. We use the centred dipole plus the off-centred quadrupole in vacuum to find the trial magnetic field configuration, which can reproduce two hotspot shapes similar to the NICER observed ones.

The centred dipole field with magnetic dipole moment  $\mathbf{m}_D = (\sin \chi_D \cos \phi_D, \cos \chi_D \sin \phi_D, \cos \chi_D)$  depicted by dipole inclination angle  $\chi_D$  and azimuth angle  $\phi_D$  is given by

$$\mathbf{B}_D = B_D \frac{R_*^3}{r^3} \left[ \frac{3(\mathbf{m}_D \cdot \mathbf{r})}{r^2} \mathbf{r} - \mathbf{m}_D \right], \quad (1)$$

Where  $B_D$  is surface dipole magnetic field,  $R_*$  is the neutron star radius.

The aligned off-centred quadrupole field with magnetic quadrupole moment  $\mathbf{m}_Q = 0$  is given by

$$\mathbf{B}_Q = B_Q \frac{R_*^4}{|\mathbf{r} - \mathbf{r}_Q|^4} \left\{ \frac{1}{2} (3 \cos^2 \theta - 1), \cos \theta \sin \theta, 0 \right\}, \quad (2)$$

where  $B_Q = f_{QD} B_D$  is surface quadrupole magnetic field,  $\mathbf{r}_Q = (x_Q, y_Q, z_Q)$  is the position vector of the off-centred quadrupole. For the oblique off-centred quadrupole field with  $\mathbf{m}_Q = (\sin \chi_Q \cos \phi_Q, \cos \chi_Q \sin \phi_Q, \cos \chi_Q)$  depicted by quadrupole inclination angle  $\chi_Q$  and azimuth angle  $\phi_Q$ , we rotate the coordinates in the  $(\chi_Q, \phi_Q)$  angles to the aligned off-centred quadrupole field, the oblique off-centred quadrupole field is then obtained by rotating the aligned quadrupole field in the  $(\phi_Q, \chi_Q)$  angles.

### 2.2. FF+AE Dipole Magnetospheres

The FF+AE magnetospheres are described by the time-dependent Maxwell equations in the rotating coordinate system (Muslimov & Harding 2005; Pétri 2020b)

$$\frac{\partial \mathbf{B}}{\partial t'} = -\nabla \times (\mathbf{E} + \mathbf{V}_{\text{rot}} \times \mathbf{B}), \quad (3)$$

$$\frac{\partial \mathbf{E}}{\partial t'} = \nabla \times (\mathbf{B} - \mathbf{V}_{\text{rot}} \times \mathbf{E}) - \mathbf{J} + \mathbf{V}_{\text{rot}} \nabla \cdot \mathbf{E}, \quad (4)$$

$$\nabla \cdot \mathbf{B} = 0, \quad (5)$$

$$\nabla \cdot \mathbf{E} = \rho_e, \quad (6)$$

where  $\rho_e$  is the charge density,  $\mathbf{V}_{\text{rot}} = \boldsymbol{\Omega} \times \mathbf{r}$  is the corotating velocity. The FF+AE current density  $\mathbf{J}$  is defined

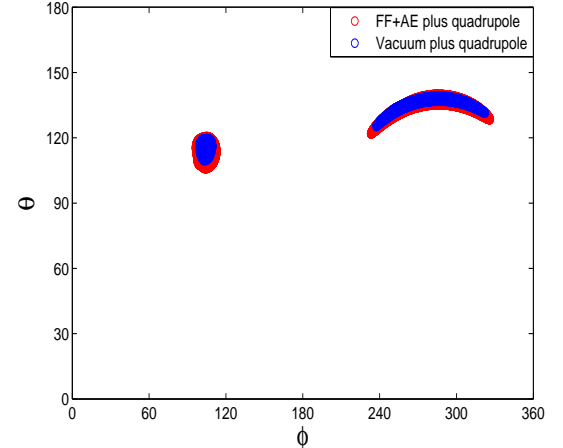


**Figure 1.** The polar caps from the FF+AE dipole plus off-centred quadrupole fields (the red curves) and the vacuum dipole plus off-centred quadrupole fields (the blue curves).

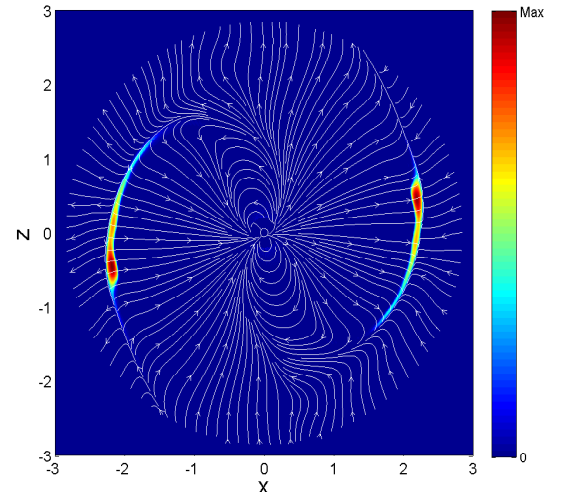


**Figure 2.** The Distribution of the magnetic field lines and the accelerating electric fields from the FF+AE dipole plus off-centred quadrupole field.

by introducing the pair multiplicity  $\kappa$  (Cao & Yang 2020)

$$\mathbf{J} = \rho_e \frac{\mathbf{E} \times \mathbf{B}}{B^2 + E_0^2} + (1 + \kappa) |\rho_e| \frac{(B_0 \mathbf{B} + E_0 \mathbf{E})}{B^2 + E_0^2}, \quad (7)$$

where  $B_0$  and  $E_0$  are the electromagnetic field strength in the frame where  $\mathbf{E}$  and  $\mathbf{B}$  are parallel, and  $E_0$  is the effective accelerating electric component  $E_{\text{acc}}$ . The quantities  $B_0$  and  $E_0$  are deduced from the electromagnetic invariants

$$B_0^2 - E_0^2 = \mathbf{B}^2 - \mathbf{E}^2, \quad E_0 B_0 = \mathbf{E} \cdot \mathbf{B}, \quad E_0 \geq 0. \quad (8)$$

A 3D spectral method is used to solve the time-dependent Maxwell equations with the FF+AE current density in the rotating coordinate system (Cao & Yang

2022). The initial magnetic field is set to be an oblique vacuum dipole with magnetic inclination angles  $\chi_D$  from  $0^\circ$  to  $90^\circ$  with a  $5^\circ$  interval. A combined three order Runge–Kutta and Adam–Bashforth method is used to advance the electromagnetic field at each time step. A rotating electric field  $\mathbf{E} = -(\mathbf{\Omega} \times \mathbf{r}) \times \mathbf{B}$  is used to impose the inner boundary condition at the stellar surface. A outgoing boundary condition is implemented to prevent inward reflection from the artificial outer boundary. A high pair multiplicity  $\kappa = 3$  is chosen to produce a near FF solution with the accelerating electric field in the current sheet outside the light cylinder. The FF+AE magnetospheres is constructed by applying the FF description where  $E \leq B$  and the AE description where  $E > B$ . A high resolution of  $N_r \times N_\theta \times N_\phi = 257 \times 64 \times 128$  is used to obtain the high-precision FF+AE magnetosphere from the stellar surface  $r = 0.2 R_L$  to  $r = 3 R_L$ . The FF+AE magnetosphere stabilizes to a near FF solution for a higher  $\kappa > 3$  value, but the accelerating electric field  $E_{\text{acc}}$  decreases with increasing  $\kappa$  (see Cao & Yang 2022). Therefore, we compute the  $E_{\text{acc}}$  value at  $\kappa > 3$  by a scaling relation (Cao & Yang 2024b)

$$E_{\text{acc}} = E_{\text{acc},0} \frac{\kappa_0}{\kappa} \quad (\kappa > \kappa_0) \quad (9)$$

where  $E_{\text{acc},0}$  corresponds to the accelerating electric field at  $\kappa_0 = 3$ .

### 2.3. Magnetospheric Configuration

There are 8 free parameters in our magnetospheric model, they are  $(\chi_D, \phi_D, \chi_Q, \phi_Q, x_Q, y_Q, z_Q, f_{QD})$ . To reduce the free parameters, we place the off-centred quadrupole position to the z-axis with  $\mathbf{r}_Q = (0, 0, z_Q)$ , and magnetic dipole moment is placed to the x–z plane with  $\phi_D = 0$ . Therefore, the total model parameters are reduced to the 5 free parameters of  $(\chi_D, \chi_Q, \phi_Q, z_Q, f_{QD})$ , which defines the magnetic field configuration with minimum free parameters. The neutron star surface is randomly discretized in the  $(\theta, \phi)$  directions with a surface resolution of  $5000 \times 5000$ , a fourth order Runge–Kutta method is used to find the open magnetic line regions on the stellar surface.

We use the vacuum dipole plus off-centred quadrupole fields with minimum parameter assumption to find a range of initial free parameters with polar caps similar to the NICER results. Figure 1 shows an example of the polar caps from the vacuum dipole plus off-centred quadrupole fields. The model parameters are  $\chi_D = 75^\circ$ ,  $\chi_Q = 53^\circ$ ,  $\phi_Q = 185^\circ$ ,  $z_Q = -0.05 R_*$ ,  $f_{QD} = 5$ . Our model can produce two hotspots with a almost circular shape and a crescent shape in the southern hemisphere, and the two hotspots are approximately spaced by  $\sim$

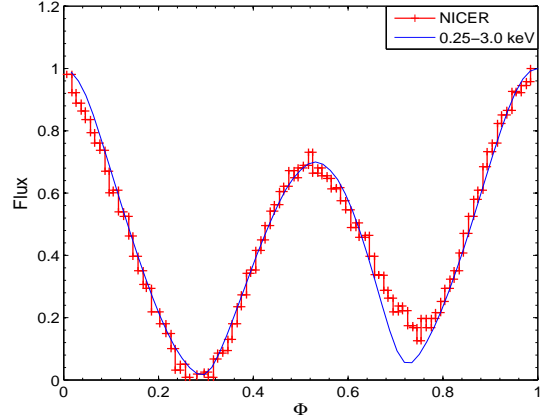


**Figure 3.** A comparison of the predicted X-ray light curves and the NICER observed ones for PSR J0030+0451. The NICER observed data is taken from Bogdanov et al. (2019).

$180^\circ$  in the  $\phi$  direction. Our hotspot configurations are similar to the NICER observed ones.

These initial parameters are then used to construct the FF+AE dipole plus off-centred quadrupole magnetospheres, which can include the modification of plasma charges currents on the polar caps. Figure 1 also shows the polar caps from the FF+AE dipole plus off-centred quadrupole fields. It is found that the polar caps from the FF+AE dipole plus off-centred quadrupole fields are similar to the vacuum dipole plus off-centred quadrupole ones, but they are more larger and more shifted than the vacuum dipole plus off-centred quadrupole ones due to the modification of magnetospheric plasmas on the polar caps. Figure 2 shows the distribution of magnetic field lines and accelerating electric fields  $E_{\text{acc}}$  from the FF+AE dipole plus off-centred quadrupole magnetosphere in the  $x$ – $z$  plane. The magnetic field lines originate from the two polar caps both in the southern hemisphere. The global field structures are similar to the FF dipole solutions with the current sheet outside the light cylinder, and the accelerating electric fields are only confined in the region near the current sheet.

### 3. RAY-TRACING METHOD FOR X-RAYS

The pulsar X-ray thermal emission can be computed by performing the ray-tracing of the emitting photons from hot spots on the surface of the neutron star. We use a forward ray-tracing method to trace the photon paths from the emitting region to observer in the spherical Schwarzschild metrics (see Poutanen & Beloborodov 2006; Bogdanov et al. 2007). A surface hot spot is defined at the co-latitude  $\theta$  and azimuthal angle  $\phi$  with the unit vector of  $\mathbf{n} = (\sin \theta \cos \phi, \sin \theta \sin \phi, \cos \theta)$ . A distant observer is placed at the  $x$ – $z$  plane with the unit vector of  $\mathbf{k} = (\sin \zeta, 0, \cos \zeta)$ , where  $\zeta$  is the inclination of the line of sight to the spin axis. The deflection angle

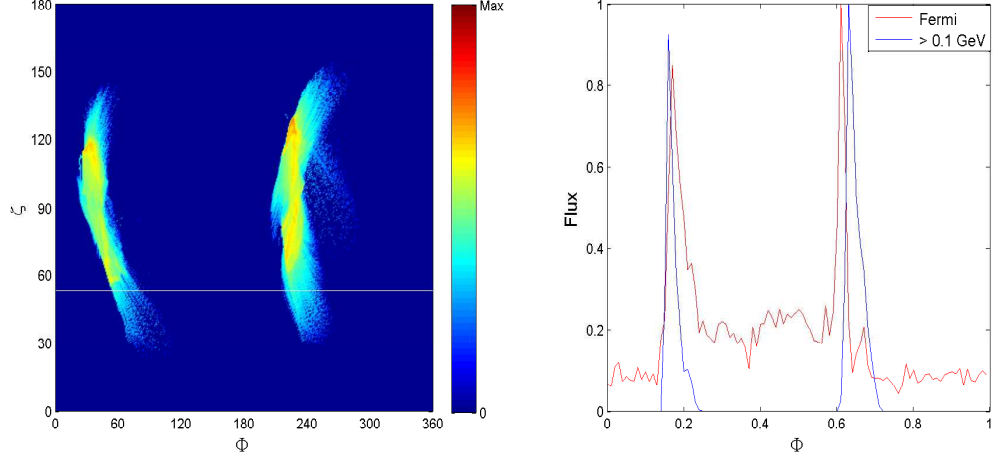


**Figure 4.** The sky maps and a comparison of the predicted  $\gamma$ -ray light curves and the Fermi observed ones for PSR J0030+0451. The Fermi observed data is taken from data taken from [Abdo et al. \(2013\)](#).

between the direction of the hot spot and the line of sight is given by

$$\cos \psi = \mathbf{k} \cdot \mathbf{n} = \cos \zeta \cos \theta + \sin \zeta \sin \theta \cos \phi. \quad (10)$$

The relation between the deflection angle  $\psi$  and the photon emission angle  $\alpha$  is given by ([Lo et al. 2013; Salmi et al. 2018](#))

$$\psi = 2 \frac{\sin \alpha}{\sqrt{1-u}} \int_0^1 \frac{xdx}{\sqrt{x^2q + \cos^2 \alpha}}, \quad (11)$$

where  $q = [2-x^2-u(1-x^2)^2/(1-u)] \sin^2 \alpha$ ,  $u = R_s/R_*$ ,  $R_s = 2GM/c^2$  is the Schwarzschild radius. The time delay from the light bending is given by ([Lo et al. 2013; Salmi et al. 2018](#))

$$\Delta t_{\text{ret}} = 2 \frac{R_* \sin^2 \alpha}{c} \int_0^1 \frac{xdx}{\sqrt{x^2q + \cos^2 \alpha} (1 + \sqrt{x^2q + \cos^2 \alpha})} \quad (12)$$

The observed flux from the area element  $dS$  at the source distance  $D$  is given by ([Beloborodov 2002; Poutanen & Beloborodov 2006](#))

$$F(E) = \sqrt{1-u} \delta^3 I'(E', \alpha') \cos \alpha \frac{d \cos \alpha}{d \cos \psi} \frac{dS}{D^2}, \quad (13)$$

where  $\cos \alpha' = \delta \cos \alpha$ , and  $E' = E/(\delta \sqrt{1-u})$ ,  $E'$  is the photon energy in the co-rotating frame,  $I'(E', \alpha')$  is the specific intensity intensity of the emission in the co-rotating frame,  $\delta$  is the Doppler factor with

$$\delta = \frac{1}{\Gamma(1 - \beta \cos \xi)}, \quad (14)$$

where  $\Gamma = \sqrt{1 - \beta^2}$ ,  $\beta = v/c$  is the spot velocity with

$$v = \frac{2\pi R_*}{P\sqrt{1-u}} \sin \alpha. \quad (15)$$

The angle  $\xi$  between the photon emission direction and the spot velocity direction is given by

$$\cos \xi = -\frac{\sin \alpha}{\sin \psi} \sin \zeta \sin \phi, \quad (16)$$

The X-ray emission from hot spots is approximated as the blackbody spectrum with the uniform temperature  $T'$  in the co-rotating frame by

$$I'(E', \alpha') = \frac{2}{c^2 h^3} \frac{E'^3}{e^{E'/kT'} - 1} \mathcal{B}(\alpha'), \quad (17)$$

where  $T' = \Gamma T$ , and an anisotropy beaming distribution is introduced to approximate the atmosphere model given by

$$\mathcal{B}(\alpha) = \cos^b \alpha, \quad (18)$$

where  $b$  is the anisotropy index, and  $b \sim 0.5 - 1.0$  is a good approximation to the atmosphere model ([Kalapotharakos et al. 2021](#)). We find that the NICER X-ray profile of PSR J0030+0451 can be well reproduced for  $b = 0.65$ .

The photon emission direction  $\mathbf{k}_0$  is given by

$$\mathbf{k}_0 = \frac{\sin \alpha \mathbf{k} + \sin(\psi - \alpha) \mathbf{n}}{\sin \psi}. \quad (19)$$

The observed phase is determined by including the rotation and time delay effects

$$\phi_{\text{obs}} = \phi_{\text{em}} + \Omega \Delta t_{\text{ret}} - \phi_{\text{rot}} \quad (20)$$

where  $\phi_{\text{em}}$  is the phase of the emitting photon,  $\phi_{\text{rot}} = \Omega \Delta t$  is the rotation phase.

The hot spots are randomly discretized into a series of small area element in the  $(\theta, \phi)$  grids. We use a forward

ray-tracing method to compute the photon emission direction and the X-ray flux from each small area element. The X-ray light curves is constructed by accumulating all the X-ray flux from each small area element at a constant view angle  $\zeta$ .

#### 4. PARTICLE TRAJECTORY METHOD FOR $\gamma$ -RAYS

The pulsar  $\gamma$ -ray emission can be computed by tracing the particle radiation with particle trajectory method in the dissipative magnetosphere. The particle trajectory is defined as the AE velocity formula by (Gruzinov 2012; Cai et al. 2023; Pétri 2023b)

$$\mathbf{v}_\pm = \frac{\mathbf{E} \times \mathbf{B} \pm (B_0 \mathbf{B} + E_0 \mathbf{E})}{B^2 + E_0^2}, \quad (21)$$

where the two signs represent positrons and electrons. They follow different trajectories in the dissipative magnetosphere, which only depends on the local electromagnetic field. The Lorentz factor of the emitting particle is integrated by including the influence of both the local accelerating electric field and the curvature reaction

$$\frac{d\gamma}{dt} = \frac{q_e c E_{\text{acc}}}{m_e c^2} - \frac{2q_e^2 \gamma^4}{3R_{\text{CR}}^2 m_e c}. \quad (22)$$

The spectrum of the curvature radiation from individual emitting particle with Lorentz factor  $\gamma$  is given by

$$F(E_\gamma, r) = \frac{\sqrt{3}e^2 \gamma}{2\pi\hbar R_{\text{CR}} E_\gamma} F(x), \quad (23)$$

where  $x = E_\gamma/E_{\text{cur}}$ ,  $E_\gamma$  is the curvature photon energy,  $E_{\text{cur}} = \frac{3}{2}c\hbar \frac{\gamma^3}{R_{\text{CR}}}$  is the characteristic curvature photon energy, the function  $F(x)$  is defined by

$$F(x) = x \int_x^\infty K_{5/3}(\xi) d\xi, \quad (24)$$

and the curvature radius  $R_{\text{C}}$  is computed by

$$R_{\text{CR}} = \left| \frac{d\beta}{dl} \right|^{-1}. \quad (25)$$

The direction of the photon emission  $\boldsymbol{\eta}$  is locally tangent to the direction of particle motion  $\boldsymbol{\beta} = \mathbf{v}/c$ , the photon emission angles is given by

$$\mu_{\text{em}} = \beta_z, \quad \phi_{\text{em}} = \text{atan} \left( \frac{\beta_y}{\beta_x} \right), \quad (26)$$

where  $\zeta = \text{acos}(\mu_{\text{em}})$ . The observed phase is determined by including the rotation and time-delay effects

$$\phi_{\text{obs}} = \phi_{\text{em}} + \mathbf{r}_{\text{em}} \cdot \boldsymbol{\eta}_{\text{em}} / r_{\text{L}} - \Omega \Delta t. \quad (27)$$

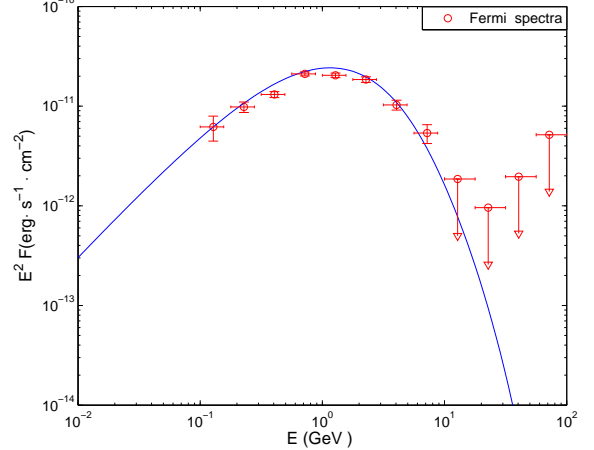


**Figure 5.** A comparison of the predicted  $\gamma$ -ray phase-averaged spectra and the Fermi observed ones for PSR J0030+0451. The Fermi observed data is taken from Abdo et al. (2013).

Positrons and electrons are randomly injected from hot spots on the surface of the neutron star. We use the particle trajectory method to compute the photon spectrum of curvature radiation and the direction of the photon emission from each emitting particle. The sky maps are constructed by accumulating all radiation photons in the  $(\zeta, \phi)$  plane. The  $\gamma$ -ray light curves and spectra is produced by cutting the sky maps at a constant view angle  $\zeta$ .

#### 5. RESULTS

The NICER X-ray emission can be used to diagnose the surface magnetic field structures, while the Fermi  $\gamma$ -ray emission can provide a probe of the outer magnetic field structures. Therefore, the combined X-ray and  $\gamma$ -ray modeling can provide a stronger constraints on the global magnetic field structures by breaking the field degeneracies. We use the polar caps in figure 1 to produce the X-ray light curves of PSR J0030+0451. The modeling parameters are chosen to be the stellar mass  $M_* = 1.34 M_\odot$ , the stellar radius  $R_* = 1.27 \times 10^6$  cm, the hotspot temperature  $T = 1.3 \times 10^6$  K and the observer angle  $\zeta = 54^\circ$ , which are same to those from the result of Riley et al. (2019). We show the predicted and NICER observed X-ray light curves in the 0.25–3.0 keV bands in Figure 3. It is find that our results can well reproduce the observed trends of the NICER X-ray light curves. The predicted double-peak X-ray profile with the phase separation of  $180^\circ$  is in good agreement with the NICER observed one.

We show the sky maps and the predicted  $\gamma$ -ray light curves from curvature radiation in the  $> 0.1$  GeV bands in Figure 4. The model parameters are  $B_* = 2.5 \times 10^8$  G,  $P = 4.87$  ms and  $\kappa = 6$ . We see that the emission pattern

from the sky map shows the characteristic of radiation with two bright caustics from the current sheet. The peak separation and the peak ratio of the Fermi  $\gamma$ -ray light curves can well be reproduced by our model. It is found that our results can well reproduce the observed trends of the Fermi  $\gamma$ -ray light curves. We also show the predicted and Fermi observed  $\gamma$ -ray phase-averaged spectra from curvature radiation in Figure 5. We see that our model can produce an exponential power-law spectrum with the  $\sim$  GeV cutoff energy by curvature radiation from the current sheet, and the predicted phase-averaged spectra provide a good match to the Fermi observed data of PSR J0030+0451. Our results suggest that the curvature radiation from the current sheet is the main radiation mechanism of Fermi  $\gamma$ -ray emission (Kalapotharakos et al. 2014; Harding et al. 2018; Cao & Yang 2024b; Íñiguez-Pascual et al. 2025).

## 6. DISCUSSION AND CONCLUSIONS

We use the dissipative FF+AE dipole plus off-centred quadrupole magnetospheres to study the X-ray and  $\gamma$ -ray emission of PSR J0030+0451. The high-resolution FF+AE dipole magnetospheres are computed by a 3D pseudo-spectral method in the rotating coordinate system. It is found that the FF+AE dipole plus off-centred quadrupole magnetosphere are similar to the FF solutions with the accelerating electric fields only near current sheet outside the LC. We then use the FF+AE dipole plus off-centred quadrupole fields with minimum free parameters to obtain the polar cap shapes, which are similar to the hotspot configuration from NICER observations. The thermal X-ray emission from two hotspots is produced by a develop ray-tracing method, and the  $\gamma$ -ray emission from curvature radiation is also simultaneously computed by a particle trajectory method based on the accelerating electric field from the FF+AE simulation. We then directly compare the modelled X-ray and  $\gamma$ -ray emission with those of PSR J0030+0451 from the NICER and Fermi observations. Our results can well reproduce the observed trends of the NICER X-ray and Fermi  $\gamma$ -ray emission for PSR J0030+0451.

The X-ray and  $\gamma$ -ray emission of PSR J0030+0451 was also simultaneously modelled by the FF dipole plus

off-centred quadrupole magnetospheres (Chen et al. 2020; Kalapotharakos et al. 2021). However, the  $\gamma$ -ray emission is not self-consistently computed by using the accelerating electric fields from magnetospheric simulations in these studies. Our model provides a more self-consistent modeling of the  $\gamma$ -ray emission by using the accelerating electric fields from the FF+AE simulations, which can both well reproduce the NICER X-ray and Fermi  $\gamma$ -ray emission of PSR J0030+0451. Our combined X-ray and  $\gamma$ -ray modeling obtain a dipole inclination angle of  $75^\circ$ , which is consistent with the result from the combined radio and  $\gamma$ -ray modeling in Pétri et al. (2023a). A dipole inclination angle of  $\sim 80^\circ$  is also found from the combined X-ray and  $\gamma$ -ray modeling in Chen et al. (2020) and Kalapotharakos et al. (2021). Therefore, we suggest a dipole inclination angle of  $70^\circ < \chi_D < 90^\circ$  as a robust estimates for PSR J0030+0451. A uniform temperature distribution from the hotspot regions is assumed in our X-ray modeling. We will include a non-uniform temperature distribution from the hotspot regions to model the X-ray emission of PSR J0030+0451 in the next step. A growing number of MSPs are expected to detected by NICER with high-precision measurement of the X-ray light curves. We will further explore the general properties of our model for a group of MSPs with the X-ray and  $\gamma$ -ray observations. The X-ray emission from MSPs may show significant polarization properties in the present of the multipolar fields. Future X-ray polarization measurement can provide an additional dimension to break the parameter degeneracy and constrain the surface magnetic field structure. We will extend our model to present the predictions of MSPs multi-wavelength radiation and polarization in the future work.

## ACKNOWLEDGMENTS

We thank the anonymous referee for valuable comments and suggestions. We would like to thank Jérôme Pétri and Joaquin Pelle for some useful discussions. We acknowledge the financial support from the National Natural Science Foundation of China 12003026, 12373045 and 12403057, and the Basic research Program of Yunnan Province 202001AU070070 and 202301AU070082.

## REFERENCES

Abdo, A. A., Ackermann, M., Atwood, W. B., et al. 2009, ApJ, 699, 1171  
 Abdo, A. A., Ajello, M., Allafort, A., et al. 2013, ApJS, 208, 17  
 Bai, X.N., & Spitkovsky, A. 2010, ApJ, 715, 1282  
 Beloborodov, A. M. 2002, ApJ, 566, L85  
 Brambilla, G., Kalapotharakos, C., Timokhin, A. N., Harding, A. K. & Kazanas, D. 2018, ApJ, 858, 81

Bogdanov, S., Rybicki, G. B., & Grindlay, J. E. 2007, *ApJ*, 670, 668

Bogdanov, S., Guillot, S., Ray, P. S., et al. 2019, *ApJL*, 887, L25

Cao, G., Zhang, L., & Sun, S. N. 2016a, *MNRAS*, 455, 4267.

Cao, G., Zhang, L., & Sun, S. N. 2016b, *MNRAS*, 461, 1068.

Cao, G., & Yang, X. B. 2019, *ApJ*, 874, 166

Cao, G., & Yang, X. B. 2020, *ApJ*, 889, 29

Cao, G., & Yang, X. B. 2022, *ApJ*, 925, 130

Cao, G., Yang, X. B., & Zhang, L. 2024a, *Universe*, 10, 130

Cao, G., & Yang, X. B. 2024b, *ApJ*, 962, 184

Carrasco, F., Palenzuela, C. & Reula, O. 2018, *Phys. Rev. D*, 98, 023010

Carrasco, F., Pelle, J., Reula, O., Viganó, D., & Palenzuela, C. 2023, *MNRAS*, 520, 3151

Cai, Y., Gralla, S. E., & Paschalidis, V. 2023, *PhRvD*, 108, 063018

Chen, A. Y., Yuan, Y., & Vasilopoulos, G. 2020, *ApJ*, 893, L38

Contopoulos, I., Kazanas, D., & Fendt, C. 1999, *ApJ*, 511, 351

Contopoulos, I., & Kalapotharakos, C. 2010, *MNRAS*, 404, 767

Contopoulos I. 2016, *MNRAS*, 463, L94

Cerutti B., Philippov A. A., & Spitkovsky, A. 2016, *MNRAS*, 457, 2401

Deutsch, A. J. 1955, *Ann. Astrophys*, 18, 1

Dimitropoulos, I. & Contopoulos, I. 2024, arXiv:2410.10716

Goldreich, P., & Julian, W. H. 1969, *ApJ*, 157, 869

Gruzinov, A. 2012, arXiv: 1205.3367

Harding, A. K., & Kalapotharakos, C. 2015, *ApJ*, 811, 63

Harding, A. K., Kalapotharakos, C., Barnard, M., & Venter, C. 2018, *ApJL*, 869, L18

Harding, A. K., Venter, C., & Kalapotharakos, C. 2021, *ApJ*, 923, 194

Íñiguez-Pascual, D., Torres, D. F., & Viganó, D., 2025, *MNRAS*, 541, 806

Kalapotharakos, C., & Contopoulos, I. 2009, *A&A*, 496, 495

Kalapotharakos, C., Kazanas D., Harding, A., & Contopoulos, I. 2012, *ApJ*, 749, 2

Kalapotharakos, C., Harding, A. K., & Kazanas, D. 2014, *ApJ*, 793, 97

Kalapotharakos, C., Brambilla, G., Timokhin, A., Harding, A. K., & Kazanas, D. 2018, *ApJ*, 857, 44

Kalapotharakos, C., Wadiasingh, Z., Harding, A. K., & Kazanas, D. 2021, *ApJ*, 907, 63

Kalapotharakos, C., Wadiasingh, Z., Harding, A. K., & Kazanas, D., 2023, *ApJ*, 954, 204

Kim, Y., Most, E. R., Throwe, W., et al. 2024, *PhRvD*, 109, 123019

Li, J., Spitkovsky, A., & Tchekhovskoy, A. 2012, *ApJ*, 746, 60

Lo, K. H., Miller, M. C., Bhattacharyya, S., & Lamb, F. K. 2013, *ApJ*, 776, 19

Muslimov, A. G., & Harding, A. K. 2005, *ApJ*, 630, 454

Miller, M. C., Lamb, F. K., Dittmann, A. J., et al. 2019, *ApJ*, 887, L24

Pétri, J. 2012, *MNRAS*, 424, 605

Pétri, J. 2016, *MNRAS*, 455, 3779

Pétri, J. 2020a, *MNRAS*, 491, 46

Pétri, J. 2020b, *Universe*, 6, 15

Pétri, J. 2022, *MNRAS*, 512, 2854

Pétri, J., Guillot, S., Guillemot, L., et al. 2023a, *A&A*, 680, 93

Pétri, J. 2023b, *A&A*, 677, 72

Pétri, J. 2025, *A&A* in press, arXiv:2104.09802

Philippov, A. A., Spitkovsky, A., & Cerutti, B. 2015, *ApJ*, 801, L19

Philippov, A. A. & Spitkovsky, A., 2018, *ApJ*, 855, 94

Poutanen, J., & Beloborodov, A. M. 2006, *MNRAS*, 373, 836

Riley, T. E., Watts, A. L., Bogdanov, S., et al. 2019, *ApJ*, 887, L21

Salmi, T., Nättilä, J., & Poutanen, J. 2018, *A&A*, 618, A161

Skiathas, D., Kalapotharakos, C., Wadiasingh, Z., et al. 2025, *ApJ*, 994, 131

Spitkovsky, A. 2006, *ApJ*, 648, L51

Soudais, S., Cerutti B., & Contopoulos, I. 2024, *A&A*, 690, A170

Yang, X. B., & Cao, G. 2021, *ApJ*, 909, 88

Yang, X. B., & Cao, G. 2024, *ApJ*, 964, 72